Broken-Symmetry States in Doubly Gated Suspended Bilayer Graphene

R. T. Weitz, *et al.*

Science **330**, 812 (2010);
DOI: 10.1126/science.1194988

This copy is for your personal, non-commercial use only.

If you wish to distribute this article to others, you can order high-quality copies for your colleagues, clients, or customers by clicking here.

Permission to republish or repurpose articles or portions of articles can be obtained by following the guidelines here.

The following resources related to this article are available online at www.sciencemag.org (this infomation is current as of December 7, 2010):

Updated information and services, including high-resolution figures, can be found in the online version of this article at:
http://www.sciencemag.org/content/330/6005/812.full.html

Supporting Online Material can be found at:
http://www.sciencemag.org/content/suppl/2010/10/13/science.1194988.DC1.html

This article appears in the following **subject collections:**
Physics, Applied
http://www.sciencemag.org/cgi/collection/app_physics

Science (print ISSN 0036-8075; online ISSN 1095-9203) is published weekly, except the last week in December, by the American Association for the Advancement of Science, 1200 New York Avenue NW, Washington, DC 20005. Copyright 2010 by the American Association for the Advancement of Science; all rights reserved. The title *Science* is a registered trademark of AAAS.

Broken-Symmetry States in Doubly Gated Suspended Bilayer Graphene

R. T. Weitz, M. T. Allen, B. E. Feldman, J. Martin, A. Yacoby*

The single-particle energy spectra of graphene and its bilayer counterpart exhibit multiple degeneracies that arise through inherent symmetries. Interactions among charge carriers should spontaneously break these symmetries and lead to ordered states that exhibit energy gaps. In the quantum Hall regime, these states are predicted to be ferromagnetic in nature, whereby the system becomes spin polarized, layer polarized, or both. The parabolic dispersion of bilayer graphene makes it susceptible to interaction-induced symmetry breaking even at zero magnetic field. We investigated the underlying order of the various broken-symmetry states in bilayer graphene suspended between top and bottom gate electrodes. We deduced the order parameter of the various quantum Hall ferromagnetic states by controllably breaking the spin and sublattice symmetries. At small carrier density, we identified three distinct broken-symmetry states, one of which is consistent with either spontaneously broken time-reversal symmetry or spontaneously broken rotational symmetry.

In mono- and bilayer graphene, an unconventional quantum Hall effect arises from the chiral nature of the charge carriers in these materials (*1*–*6*). In monolayers, the sequence of Hall plateaus is shifted by a half integer, and each Landau level (LL) is fourfold degenerate due to spin and valley degrees of freedom. The latter valley degree of freedom refers to the conduction and valence bands in single-layer graphene forming conically shaped valleys that touch at two inequivalent Dirac points. In bilayer graphene, an even richer picture emerges in the lowest LL caused by an additional degeneracy between the zeroth and first orbital LLs, giving rise to an eightfold degeneracy. Systems in which multiple LLs are degenerate give rise to broken-symmetry states caused by electron-electron interactions (*7*). Such interaction-induced broken-symmetry states in the lowest LL of bilayer graphene have been theoretically predicted (*8*, *9*) and experimentally observed (*10*–*14*), but the nature of their order parameters is still debated. For example, two possible order parameters that have been suggested for the gapped phase at filling factor $\nu = 0$ at large magnetic fields are either layer or spin polarization (*9*). Moreover, recent theoretical studies predict that even in the absence of external magnetic and electric fields, the parabolic dispersion of bilayer graphene can lead to broken-symmetry states that are induced by interactions among the charge carriers (*15*–*22*). In this work, we map out the various broken-symmetry states as a function of external magnetic and electric field. The nature of these phases can be deduced by investigating their stability under the variation of these symmetry-breaking fields.

The observation of broken-symmetry states driven by effects of interaction is hampered by the presence of disorder and requires high sample quality. We have developed a method in which bilayer graphene is suspended between a top gate electrode and the substrate. This approach allows us to combine the high quality of suspended devices with the ability to independently control electron density and perpendicular electric field $E_\perp$.

A false-color scanning electron micrograph of a typical device is shown in Fig. 1A. The suspended graphene (red) is supported by gold contacts (yellow). Suspended top gates (blue) can be designed to cover only part of the graphene (left device) or to fully overlap the entire flake (right device), including part of the contacts. We have investigated both types of devices, which show similar characteristics. The fabrication of such two-terminal devices is detailed in the Supporting Online Material (*23*) and is schematically illustrated in Fig. 1A. To improve sample quality, we current anneal (*24*, *25*) our devices in vacuum at 4 K before measurement.

The high quality of our suspended flakes is evident from the dependence of resistance versus applied electric field at zero magnetic field. As theoretically predicted (*26*–*28*) and experimentally verified in transport (*29*, *30*) and optical (*30*–*32*) experiments, an applied perpendicular electric field $E_\perp$ opens a gap $\Delta \sim dE_\perp/k$ in the otherwise gapless dispersion of bilayer graphene, as schematically shown in the lower left inset to Fig. 1B. Here, d is the distance between the graphene sheets and k is a constant that accounts for imperfect screening of the external electric field by the bilayer (*19*, *26*, *28*). The conductance of our suspended bilayer graphene sheet at 100 mK as a function of back (V_b) and top gate (V_t) voltage is shown in Fig. 1B. The opening of a field-induced band gap is apparent from the decreased conductance at the charge neutrality point with increasing applied electric field $E_\perp = (\alpha V_t - \beta V_b)/2e\varepsilon_0$. Here, α and β are the gate coupling factors for V_t and V_b, respectively, which we determine from the Landau fan in the quantum Hall regime, e is the electron charge, and ε_0 is the vacuum permittivity.

The presence of an energy gap is also illustrated by the line cut in Fig. 1C, which shows the resistance at constant $E_\perp$ as a function of total density $n = (\alpha V_t + \beta V_b)$. By varying the density, the resistance can be changed by a factor 10^3. Line traces of the maximum sheet resistance as a function of $E_\perp$ at various temperatures (Fig. 1D) illustrate the exponential dependence of the resistance on electric field, as well as a decrease in resistance with temperature. The sheet resistance at 100 mK increases by more than a factor of 2×10^3 (from 8 kilohm per square to 20 megohm per square) for $E_\perp$ between 20 and 90 mV/nm. Compared to previous measurements of dually gated graphene bilayers embedded in a dielectric (*29*), our measurements show an increase by a factor of 10^3 in resistivity at the same electric field, which is the result of the high quality of our flakes. The unexpected finding of a nonmonotonous dependence of the resistance at small applied electric field will be discussed below. The oscillations in the conductance traces shown in Fig. 1C are repeatable and result from mesoscopic conductance fluctuations. A detailed description of the temperature dependence of the resistance and of these fluctuations is presented in figs. S1 and S2 (*23*).

The evolution of different LLs in our samples at nonzero magnetic field was revealed by measuring conductance as a function of $E_\perp$. The two-terminal conductance as a function of density and electric field at various different magnetic fields (Fig. 2, A to D) shows the previously reported eightfold degeneracy of the lowest LL, which is fully lifted because of electron-electron interactions (*10*, *11*, *14*, *23*). Plateaus at $\nu = 0$, ±1, ±2, ±3 can be identified by their slope in a fan diagram. Vertical line cuts that correspond to a constant filling factor show that the conductance is quantized except at particular values of electric field, denoted by stars or dots in Fig. 2, A to D. The $\nu = 0$ state is quantized except near two values of the applied electric field (marked with dots). This value of electric field increases as the magnetic field B increases. The $\nu = \pm 2$ state is quantized for all electric fields except near $E_\perp = 0$; finally, the $\nu = \pm 4$ state is quantized for all electric fields.

A qualitative understanding of this phenomenology can be gained from a simplified scheme of the LL energies as a function of electric field (Fig. 2E, gray lines) for nonzero magnetic field. We start by neglecting the breaking of the orbital degree of freedom so that the LLs are each doubly degenerate (*6*). We assume, in accordance with theoretical predictions, that at $E_\perp = 0$ only the spin degeneracy is lifted, giving rise to a spin-polarized $\nu = 0$ quantum Hall ferromagnetic state (*9*, *19*). In (*23*), we have detailed

---

Department of Physics, Harvard University, 11 Oxford Street, Cambridge, MA 02138, USA.

*To whom correspondence should be addressed. E-mail: yacoby@physics.harvard.edu

how our experimental data support this assumed sequence of degeneracy breaking. In the lowest LL, the layer and valley index are equivalent (*6*) so that an electric field that favors one of the layers directly controls the valley-pseudospin. As a result, LLs of quantum number U (upper layer) or L (lower layer) are expected to have different slopes in electric field. At several points, marked by dots or stars in the schematic of Fig. 2E, LL crossings occur. A LL crossing is seen at $E_\perp = 0$ for both $\nu = 2$ and $\nu = -2$, and two LL crossings are seen for $\nu = 0$ at nonzero $E_\perp$. We hypothesize that these crossings are responsible for the increased conductance in our transport experiments (*33*). Figure 2E shows the LL energy, whereas we have direct control over the density of the bilayer rather than its chemical potential. However, on a quantum Hall plateau, the chemical potential lies between two LL energies, which enables us to relate our scheme in Fig. 2E to our transport data as detailed below [see fig. S3 (*23*)].

The LL crossings at zero average carrier density are marked by dots in Fig. 2. In our proposed scheme, these transitions separate a spin-polarized $\nu = 0$ state at low electric fields (I) from two layer-polarized $\nu = 0$ states at large electric fields (II) of opposite layer polarization. The line cut in Fig. 2C at constant filling factor shows that insulating $\nu = 0$ states are well developed at zero electric field and at large electric fields, but the crossover between these states is marked by a region of increased conductance. The experimentally observed large resistance of the phase at $E_\perp = 0$ (*10*, *11*) is at variance with the theoretical prediction of percolating edge modes (*34*) in the case of a spin-polarized $\nu = 0$ state. A possible reason for this discrepancy is the mixing of counter-propagating edge modes and subsequent opening of a gap (*35*).

The LL crossings at $\nu = \pm 2$ near zero electric field are marked by stars in Fig. 2. An example of such a crossing is apparent in the vertical line cut shown in Fig. 2B. There, the conductance at $\nu = \pm 2$ increases near zero electric field, which is explained in our scheme by a crossing between two LLs of identical spin polarization but opposite layer polarization. The consequence of these crossings is that only $\nu = 0$ and $\nu = \pm 4$ states occur at zero electric field, whereas layer-polarized $\nu = \pm 2$ states emerge only at finite electric field, as is apparent in the horizontal line cuts of Fig. 2B.

Assuming that the $\nu = \pm 1$ and ± 3 states are partially layer polarized (*9*), the electric field should also induce a splitting at these filling factors (inset to Fig. 2E) that is, however, more fragile and only seen at higher magnetic fields. Our simple model predicts that the $\nu = \pm 3$ state will have a crossing at zero electric field, and we attribute the increase in conductance at $E_\perp = 0$ in the left line cut in Fig. 2D to be a signature of this crossing. A line cut at $\nu = \pm 3$ at even higher magnetic field showing a better quantization is shown in fig. S4 (*23*). The $\nu = \pm 1$ state is expected to have three crossings: one at zero electric field and two near the same nonzero electric field at which the transition between the $\nu = 0$ states is observed. All three of these crossings are apparent from the regions of increased conductance in the right line cut in Fig. 2D. The observation that $\nu = \pm 1$ and ± 3 states are enhanced with electric field is an indication of their partial layer polarization. Theory nonetheless predicts that $\nu = \pm 1, \pm 2, \pm 3$ should also be seen at $E_\perp = 0$ (*9*). However, the predicted energy gaps of these states are expected to be considerably smaller than that of $\nu = 0$ and hence visible only at large magnetic field. Indeed, for $B > 4$ T, these broken-symmetry states at $E_\perp = 0$ can also be observed in our data [see fig. S4 (*23*)].

When we examine the conductance at the charge neutrality point as a function of electric and magnetic field (Fig. 3A) in more detail, we observe that regions of high conductance mark the transition between the low- and high-field $\nu = 0$ states (highlighted with dots in Fig. 2). The transition moves out to larger electric fields as the magnetic field is increased, which implies that phase I is stable at large magnetic fields and is destabilized by an electric field. This observation is also consistent with our energy diagram (Fig. 2E), which predicts that the $\nu = 0$ LL crossing will move out to higher electric fields when the

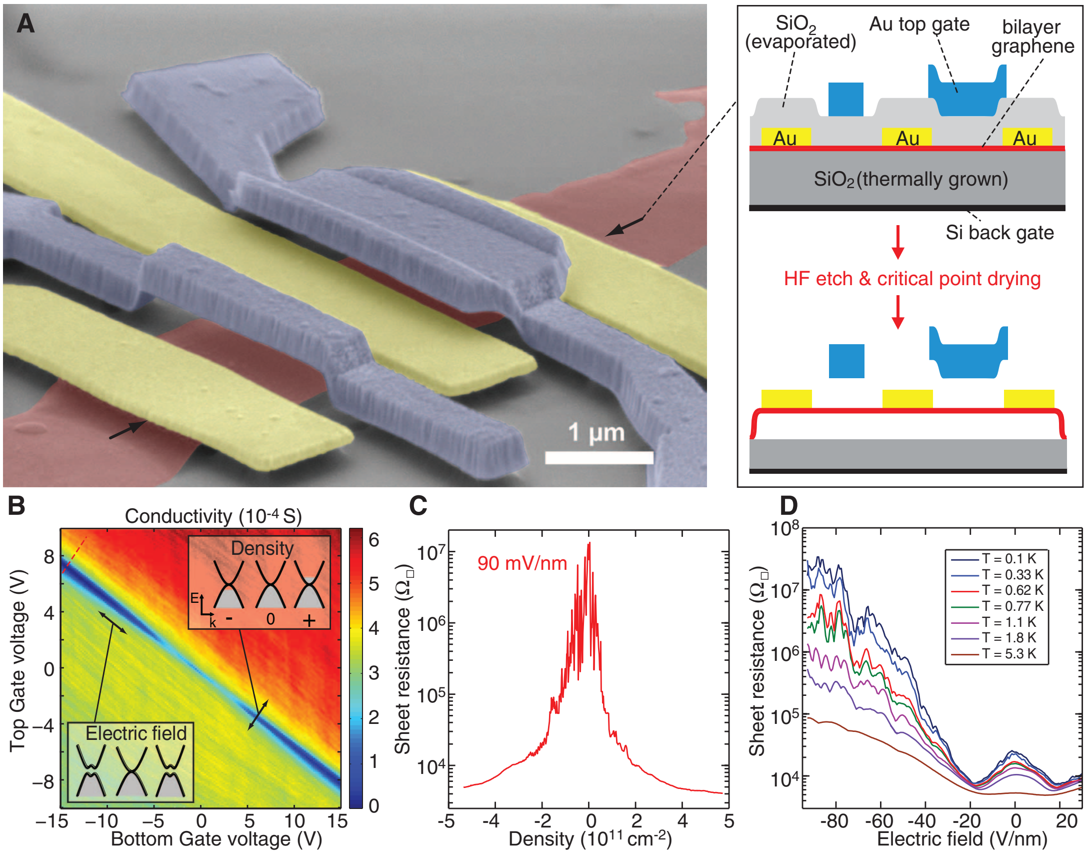

Fig. 1. (**A**) False-color scanning electron micrograph of a bilayer graphene flake suspended between Cr/Au electrodes with suspended Cr/Au top gates. A schematic of a cross section along a line marked by the two arrows is shown on the right, including a brief depiction of the sample fabrication. We used a three-step electron-beam lithography process in which Cr/Au contacts are first fabricated on the bilayer graphene, followed by deposition of a SiO$_2$ spacer layer on top of the flake and finally the structure of a Cr/Au topgate above the SiO$_2$ layer. Subsequent etching of part of the SiO$_2$ leaves the graphene bilayer suspended between the top and bottom gate electrodes. (**B**) Conductance map as function of top and bottom gate voltage at $T = 100$ mK of a suspended bilayer graphene flake. (**C**) Line trace along the dashed lines in (B) showing the sheet resistance as a function of charge carrier density at constant electric field. (**D**) Traces of the maximal sheet resistance at the charge neutrality point as a function of applied electric field at different temperatures.

magnetic field increases. The increased stability of this phase at higher magnetic fields reconfirms our initial assumption that phase I is spin polarized. In contrast, the phase at large electric fields (phase II) is stabilized by an electric field, consistent with it being layer polarized.

The dependence of the transition region between the two phases on electric and magnetic field is shown more clearly in Fig. 3B, where we have extracted the maximum conductance in Fig. 3A for all positive values of electric field. At large magnetic field, the transition line is linear and is independent of sample quality and temperature (we have investigated a total of five samples at temperatures between 100 mK and 5 K). At magnetic fields below about 2 T, however, the transition line is linear only in the highest-quality sample and at low temperatures (inset to Fig. 3A and dashed line in Fig. 3B). A surprising observation is that the extrapolation of the linear dependence from high B down to $B = 0$ results in a crossing at a nonzero electric field, E_{off}. Moreover, the slope and E_{off} that characterize the large B behavior seem to have no systematic dependence on sample quality or temperature T (Fig. 3, C and D). The conductance at the transition between the ν = 0 phases decreases both with increasing B as well as with decreasing T [see fig. S5 (*23*)]. Such behavior is qualitatively expected given that LL mixing at these crossing points can lead to the opening of gaps in the spectrum.

To further elucidate the nature of the transition, we investigated the role of the Zeeman energy E_z across the ν = 0 transition in detail. We tilted the sample with respect to the magnetic field, which altered E_z but left all interaction-dependent energy scales the same. Figure 3B shows both measurements under titled magnetic field (green line) and data taken in purely perpendicular field (blue line). The two transition lines have similar slopes, which indicates that E_z is negligible and the transition predominantly depends on the perpendicular component of the magnetic field, underscoring that exchange effects and the LL degeneracies play an important role. However, this explanation does not account for the $B = 0$ offset.

The crossover between two phases with the application of an electric field has also been predicted theoretically by Gorbar *et al.* (*36*) and Nandkishore and Levitov (*19*). Gorbar *et al.* (*36*) predict a transition from a quantum Hall ferromagnetic state at low electric fields to an insulating state dominated by magnetic catalysis with a slope of about 2 mV nm^{-1} T^{-1}. Nandkishore and Levitov (*19*) predict a transition from a quantum Hall ferromagnetic state to a layer insulating state at large electric fields, with a slope of 34 mV nm^{-1} T^{-1} . Our measured slope is about 11 mV nm^{-1} T^{-1}. A qualitative comparison between the experimentally obtained values and the theory is difficult because of the lack of knowledge of the screening that the bilayer provides to the applied electric field once LLs are formed.

A notable feature seen in the inset to Fig. 3A and in Fig. 3B is that the transition line appears to have a nonzero offset in electric field, $E_{\mathrm{off}} \approx 20$ mV/nm. The $B = 0$ offset coincides with the extrapolated one from high fields when the sample quality is high and the temperature is low. This result suggests that the transition from a spin- to a layer-polarized phase persists all the way down to $B = 0$, but careful measurements near $B = 0$ and $E_\perp = 0$ (Fig. 4A) show that this conclusion is incorrect. We will discuss possible origins for E_{off} in the remainder of this manuscript.

The conductance close to the charge neutrality point at small electric and magnetic fields is shown in Fig. 4A. The conductance at $B = 0$ and $E_\perp = 0$ exhibits a local minimum and increases upon increase of $E_\perp$ and B. The electric field value at which the conductance reaches a maximum coincides with E_{off}. Together with observation of a maximum of the conductance at a finite value $B_{\mathrm{off}} = \pm 50$ mT, our observations suggest that neither the spin-polarized phase I nor the layer-polarized phase II extend down to $B = 0$ and $E_\perp = 0$. Instead, our measurements are consistent with the presence of a third phase at small electric and magnetic fields. The electric field dependence of the resistance is at variance with simple calculations of the band structure of bilayer graphene. In a tight binding model, bilayer graphene is expected to evolve from a gapless semimetal to a gapped semiconductor whose gap magnitude depends monotonically

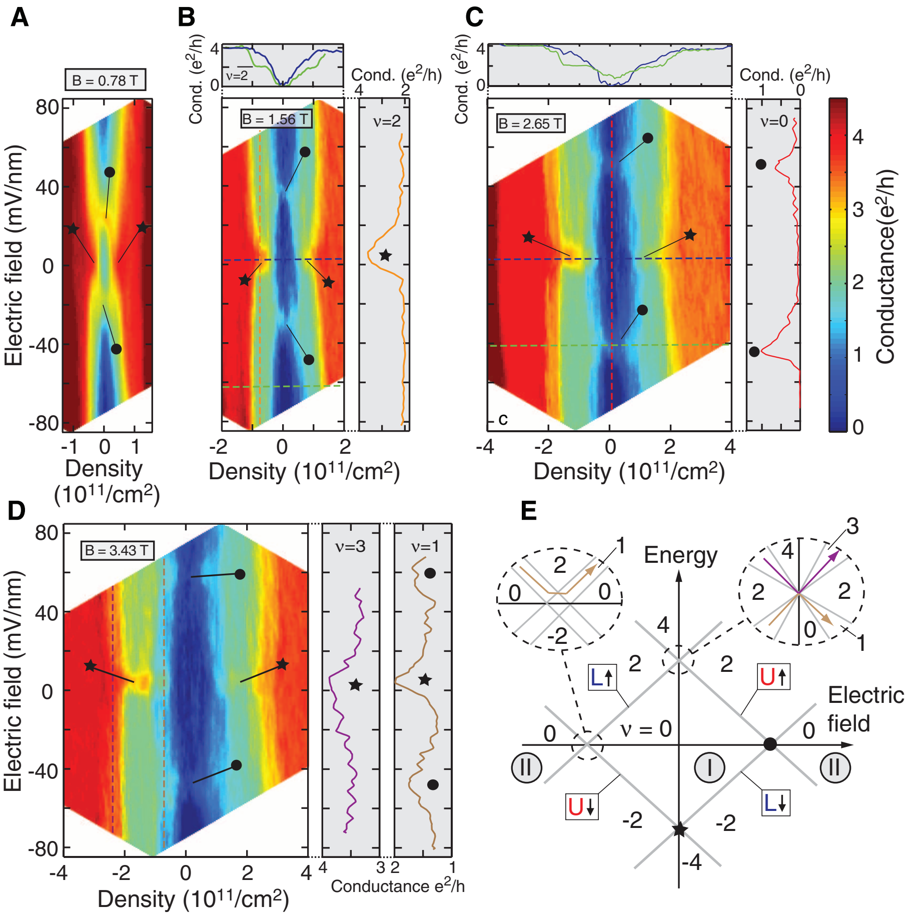

Fig. 2. (**A** to **D**) Maps of the conductance in units of e^2/h as a function of applied electric field $E_\perp$ and density n at various constant magnetic fields at T = 60 mK. Line traces are taken from the data along the dashed lines. Horizontal line traces correspond to cuts at constant electric field; vertical line cuts correspond to cuts along constant filling factor. In (**B**), the orange line cut corresponds to the electric field dependence of ν = 0 and the vertical line cuts to the density dependence of the conductance at two constant electric fields showing the emergence of ν = 2 at large electric fields. In (**C**), the red vertical line cut corresponds to the electric field dependence of ν = 0. The horizontal line cuts in green and blue show the density dependence of the conductance at two different electric fields showing the suppression of the ν = 0 state at a finite electric field. In (**D**), the brown (violet) line cut shows the conductance as function of electric field at ν = 1 (ν = 3). (**E**) Schematic diagram of the energetic position of the lowest LL octet (gray lines) as a function of $E_\perp$. The quantum numbers U, L, ↑, and ↓ of the LLs are indicated in the squares. The respective filling factors ν are indicted in black numbers. The LLs in the main scheme are all doubly degenerate in orbital quantum numbers. The effect of the electric field on the orbital LLs is shown in the two insets. The two different ν = 0 states are marked with Roman numerals. In all images, the crossing of LLs at zero electric field is marked with a star and the crossing at zero energy is marked with a dot.

on electric field (*26*). However, our measurements show that the conductance does not decrease monotonically with electric field, instead exhibiting a local maximum at about ±20 mV/nm (Fig. 4B). The maximum resistance at $B = 0$ and close to zero carrier density as a function of $E_\perp$ for different temperatures increases as T decreases [see Fig. 1D and fig. S8 (*23*)], reaching 20 kilohm at the lowest temperature of 100 mK. It therefore strongly suggests that the neutral bilayer graphene system is already gapped at $E_\perp = 0$ and $B = 0$ and that fields larger than E_{off} or B_{off} transfer the system into the layer- or spin-polarized phases (Fig. 4A). In Fig. 4B, the dependence of the conductance as a function of density and electric field at $B = 0$ is shown. Also in this case, a minimum of the conductance at small electric field and density can be discerned, indicating that the spontaneous phase is unstable away from the charge neutrality point. Further experimental evidence for phase III in different samples is given in figs. S6 and S7 (*23*). The temperature dependence at the crossover field of $E_\perp = \pm 20$ mV/nm is weak (Fig. 1D), consistent with the closure of a gap. Our observations cannot be explained with known single-particle effects, as detailed in (*23*).

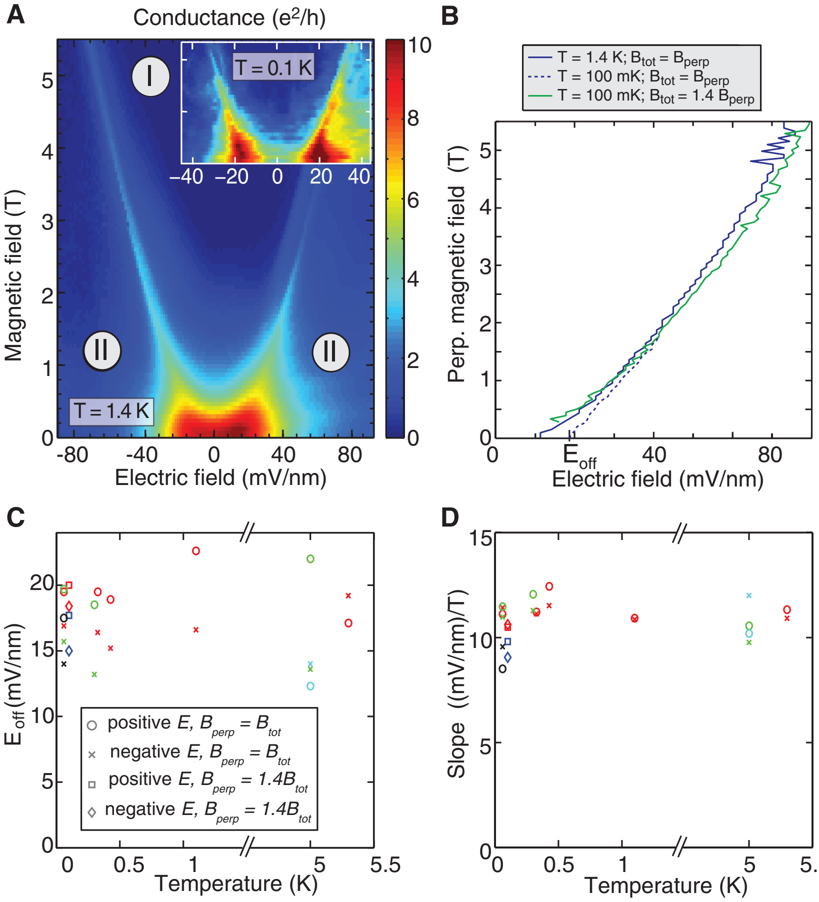

Fig. 3. (**A**) Conductance in units of e^2/h as a function of applied electric and magnetic fields at zero average carrier density at 1.4 K. The transition between different $\nu = 0$ states is characterized by a region of increased conductance. (Inset) Measurement taken at 100 mK when the sample has been tilted with respect to the magnetic field, plotted against the perpendicular component of the magnetic field after thermal cycling. The color scale of the inset ranges from 0 (blue) to 4.5 (red) e^2/h. The y axis of the inset ranges from 0 to 1.3 T. (**B**) Comparison of the slope of the transition line when the sample is perpendicular to the magnetic field and at a 45° angle. (**C** and **D**) Comparison of the E_{off} and high–magnetic field slope of the transition line for different temperatures. Different colors correspond to different samples.

It has been pointed out theoretically (*15*–*22*) that electron-electron interactions can open a spontaneous gap in bilayer graphene near the charge neutrality point at zero electric and magnetic fields. Several different phases have been proposed, and our experimental observations considerably restrict the various possible theoretical explanations to two prevailing theories. The first theory (*19*) predicts a phase diagram very similar to what we measure. Within this theory, phase III is associated with an anomalous quantum Hall insulating state that spontaneously breaks time-reversal symmetry. This state is characterized by an antiferromagnetic ordering in the pseudospin (layer). In this phase, electrons from one valley occupy one of the layers, whereas electrons from the other valley occupy the other layer. An important feature of this state is that it supports topologically protected current-carrying edge modes and is therefore predicted to have a finite conductance. This prediction is consistent with our observations of a nondiverging resistance at $B = 0$ and $E_\perp = 0$ as T is lowered [see fig. S8 (*23*)]. Although our observed phase diagram agrees qualitatively with that predicted in (*19*), we find a quantitative disagreement between the measured and predicted E and B

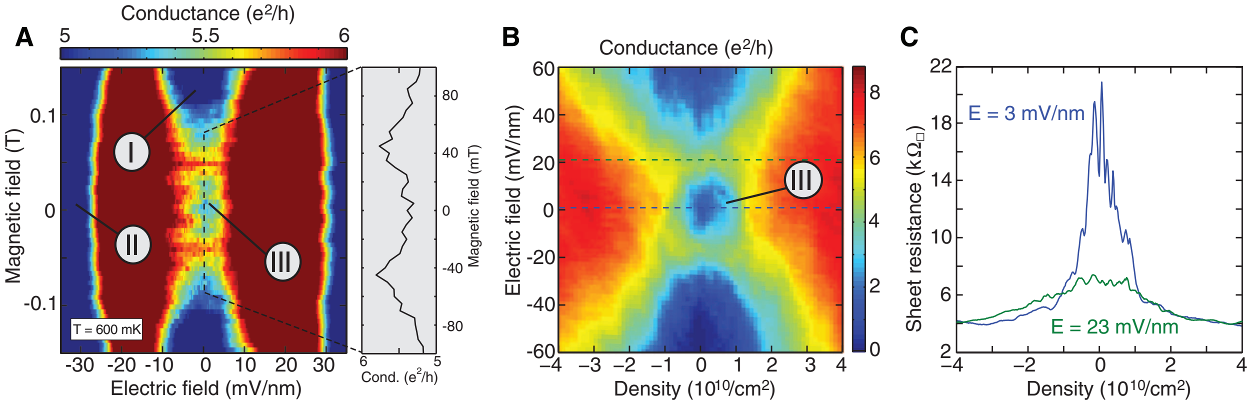

Fig. 4. Experimental evidence of a spontaneous gap in suspended bilayer graphene. (**A**) Detailed view of the conductivity at small electric and magnetic fields and zero average carrier density. The color scale has been restricted to between 5 and 6 e^2/h to highlight the observed effect. (**B**) Conductivity as a function of electric field and density at zero magnetic field. (**C**) Two linecuts showing the resistivity at $E = 0$ and E_{off} are also shown. The scans in (B) and (C) were taken after thermal cycling of the sample, hence the difference in the minimal conductance at zero magnetic and electric field with respect to (A).

transition values. We find that the magnetic field at which the spontaneous phase breaks down is about 50 mT, an order of magnitude smaller than the theoretically predicted value of 500 mT (*19*). An applied electric field of about $E_{\mathrm{off}} = 20$ mV/nm quenches the spontaneous gap, compared to the predicted value of 26 mV/nm for the screened electric field. Notably, we need to scale our measured E_{off} by the screening constant k, which means that our values differ by roughly a factor $k = 3$ from the theory (*19*). A second prevailing theory for the observed behavior stems from symmetry breaking, which results in the lowering of the density of states at the charge neutrality point. One such example is the nematic state that stems from the breaking of rotational symmetry due to electron-electron interactions. This phase has been predicted to lead to a decreased density of states at the charge neutrality point due to the breaking of the system into two Dirac cones (*21*, *22*), consistent with our measured decrease in conductance at small densities. Further experimental support for the above two scenarios is given in (*13*) and elaborated in (*23*), where it is shown that known single-particle effects cannot explain the observed behavior.

References and Notes

1. K. S. Novoselov *et al.*, *Nature* **438**, 197 (2005).
2. Y. B. Zhang, Y. W. Tan, H. L. Stormer, P. Kim, *Nature* **438**, 201 (2005).
3. K. S. Novoselov *et al.*, *Nat. Phys.* **2**, 177 (2006).
4. A. K. Geim, K. S. Novoselov, *Nat. Mater.* **6**, 183 (2007).
5. A. H. Castro Neto, F. Guinea, N. M. R. Peres, K. S. Novoselov, A. K. Geim, *Rev. Mod. Phys.* **81**, 109 (2009).
6. E. McCann, V. I. Fal'ko, *Phys. Rev. Lett.* **96**, 086805 (2006).
7. K. Yang *et al.*, *Phys. Rev. Lett.* **72**, 732 (1994).
8. M. Ezawa, *J. Phys. Soc. Jpn.* **76**, 094701 (2007).
9. Y. Barlas, R. Côté, K. Nomura, A. H. MacDonald, *Phys. Rev. Lett.* **101**, 097601 (2008).
10. B. E. Feldman, J. Martin, A. Yacoby, *Nat. Phys.* **5**, 889 (2009).
11. Y. Zhao, P. Cadden-Zimansky, Z. Jiang, P. Kim, *Phys. Rev. Lett.* **104**, 066801 (2010).
12. W. Bao *et al.*, http://arxiv.org/abs/1005.0033v1 (2010).
13. J. Martin, B. E. Feldman, R. T. Weitz, M. T. Allen, A. Yacoby, http://arxiv.org/abs/1009.2069v1 (2010).
14. C. R. Dean *et al.*, *Nat. Nanotech.* **5**, 733 (2010).
15. F. D. M. Haldane, *Phys. Rev. Lett.* **61**, 2015 (1988).
16. S. Raghu, X.-L. Qi, C. Honerkamp, S.-C. Zhang, *Phys. Rev. Lett.* **100**, 156401 (2008).
17. H. Min, G. Borghi, M. Polini, A. H. MacDonald, *Phys. Rev. B* **77**, 041407 (2008).
18. R. Nandkishore, L. S. Levitov, http://arxiv.org/abs/0907.5395v1 (2009).
19. R. Nandkishore, L. S. Levitov, http://arxiv.org/abs/1002.1966v1 (2010).
20. F. Zhang, H. Min, M. Polini, A. H. MacDonald, *Phys. Rev. B* **81**, 041402 (2010).
21. O. Vafek, K. Yang, *Phys. Rev. B* **81**, 041401 (2010).
22. Y. Lemonik, I. L. Aleiner, C. Toke, V. I. Fal'ko, http://arxiv.org/abs/1006.1399v1 (2010).
23. Supporting online material is available on *Science* Online.
24. J. Moser, A. Barreiro, A. Bachtold, *Appl. Phys. Lett.* **91**, 163513 (2007).
25. K. I. Bolotin *et al.*, *Solid State Commun.* **146**, 351 (2008).
26. E. McCann, *Phys. Rev. B* **74**, 161403(R) (2006).
27. E. V. Castro *et al.*, *Phys. Rev. Lett.* **99**, 216802 (2007).
28. H. K. Min, B. Sahu, S. K. Banerjee, A. H. MacDonald, *Phys. Rev. B* **75**, 155115 (2007).
29. J. B. Oostinga, H. B. Heersche, X. L. Liu, A. F. Morpurgo, L. M. K. Vandersypen, *Nat. Mater.* **7**, 151 (2008).
30. Y. B. Zhang *et al.*, *Nature* **459**, 820 (2009).
31. A. B. Kuzmenko *et al.*, *Phys. Rev. B* **79**, 115441 (2009).
32. K. F. Mak, C. H. Lui, J. Shan, T. F. Heinz, *Phys. Rev. Lett.* **102**, 256405 (2009).
33. Y. P. Shkolnikov, E. P. De Poortere, E. Tutuc, M. Shayegan, *Phys. Rev. Lett.* **89**, 226805 (2002).
34. D. A. Abanin *et al.*, *Phys. Rev. Lett.* **98**, 196806 (2007).
35. E. Shimshoni, H. A. Fertig, G. V. Pai, *Phys. Rev. Lett.* **102**, 206408 (2009).
36. E. V. Gorbar, V. P. Gusynin, V. A. Miransky, *Phys. Rev. B* **81**, 155451 (2010).

37. We acknowledge discussions with R. Nandikshore, L. Levitov, M. Rudner, S. Sachdev, B. I. Halperin, A. H. MacDonald, and G. Barak and experimental help by S. Foletti. R.T.W. acknowledges financial support of the Alexander von Humboldt Foundation. M.T.A. acknowledges financial support from the U.S. Department of Energy Office of Science Graduate Fellowship (DOE SCGF) administered by the Oak Ridge Institute for Science and Education (ORISE). This work was supported by the U.S. DOE, Office of Basic Energy Sciences, Division of Materials Sciences and Engineering under award #DE-SC0001819 (R.T.W., M.T.A., and B.E.F.); by the 2009 U.S. Office of Naval Research Multi University Research Initiative (MURI) on Graphene Advanced Terahertz Engineering (Gate) at Massachusetts Institute of Technology, Harvard, and Boston University (J.M.); and by Harvard's Nanoscale Science and Engineering Center under NSF award PHY-0646094. The authors declare that they have no competing financial interests.

Supporting Online Material

www.sciencemag.org/cgi/content/full/science.1194988/DC1
Materials and Methods
SOM Text
Figs. S1 to S8
References

12 July 2010; accepted 4 October 2010
Published online 14 October 2010;
10.1126/science.1194988
Include this information when citing this paper.

Efficient Atmospheric Cleansing of Oxidized Organic Trace Gases by Vegetation

T. Karl,[1]* P. Harley,[1] L. Emmons,[1] B. Thornton,[2] A. Guenther,[1] C. Basu,[2] A. Turnipseed,[1] K. Jardine[3]

The biosphere is the major source and sink of nonmethane volatile organic compounds (VOCs) in the atmosphere. Gas-phase chemical reactions initiate the removal of these compounds from the atmosphere, which ultimately proceeds via deposition at the surface or direct oxidation to carbon monoxide or carbon dioxide. We performed ecosystem-scale flux measurements that show that the removal of oxygenated VOC via dry deposition is substantially larger than is currently assumed for deciduous ecosystems. Laboratory experiments indicate efficient enzymatic conversion and potential up-regulation of various stress-related genes, leading to enhanced uptake rates as a response to ozone and methyl vinyl ketone exposure or mechanical wounding. A revised scheme for the uptake of oxygenated VOCs, incorporated into a global chemistry-transport model, predicts appreciable regional changes in annual dry deposition fluxes.

Large quantities of nonmethane volatile organic compounds (NMVOCs) enter the atmosphere via biogenic, pyrogenic, and anthropogenic sources. The annual production of NMVOCs [~ 1200 to 1350 teragrams of carbon (TgC)/year) probably exceeds that of methane and carbon monoxide (CO) (~500 TgC/year each) (*1*, *2*). Together, these gases fuel tropospheric chemistry. Oxidation of NMVOCs leads to the formation of aerosols (*3*–*5*) and modulates the oxidation capacity of the atmosphere (*6*), creating important climate feedbacks (*7*). One large uncertainty in constraining budgets of NMVOCs is the amount of deposition to vegetation, which acts as a major source and sink for organic trace gases on a global scale. This has consequences for constraining secondary species produced in the gas phase, which will either oxidize to CO and carbon dioxide (CO_2), condense onto or form organic aerosol (OA) and be rained out, or directly deposit to the surface via dry and wet deposition. Two recent bottom-up assessments of the tropospheric organic aerosol budget (*1*, *3*), on the basis of different assumptions for wet and dry deposition of organic vapors, resulted in different predictions of global production rates for secondary organic aerosol (SOA).

Dry deposition schemes parameterize the deposition flux according to

$$F = v_{\mathrm{d}} \times C \tag{1}$$

where F represents the deposition flux, C is the ambient concentration, and v_{d} is the deposition velocity. Deposition velocities are usually treated in analogy to Ohm's Law, where v_{d} can be expressed as three resistances in series:

$$v_{\mathrm{d}} = \frac{1}{R_{\mathrm{a}} + R_{\mathrm{b}} + R_{\mathrm{c}}} \tag{2}$$

R_{a} represents the aerodynamic resistance above the surface and has the same value for all constituents. The term R_{b} is the quasi-laminar resistance to transport through the thin layer of air in

---

[1] National Center for Atmospheric Research, Boulder, CO 80301, USA. [2] School of Biological Sciences, University of Northern Colorado, Greeley, CO 80639, USA. [3] Biosphere 2, University of Arizona, Tucson, AZ 85738, USA.

*To whom correspondence should be addressed. E-mail: tomkarl@ucar.edu